RESEARCH ARTICLE

Open Access

Quasicrystal metasurface for dual functionality of holography and diffraction generation

Chi Xu[1], Ruizhe Zhao[1], Xue Zhang[1], Shifei Zhang[1], Xin Li[1], Guangzhou Geng[2], Junjie Li[2], Xiaowei Li[3], Yongtian Wang[1] and Lingling Huang[1*]

Abstract

Quasicrystal has attracted lots of attention since its discovery because of the mathematically non-periodic arrangement and physically unique diffraction patterns. By combining the quasi-periodic features of quasicrystal and the special rotational symmetry with metasurface, many novel phenomena and applications are proposed such as optical spin-Hall effect, non-linear far-field radiation control, and broadband polarization conversion. However, the additional functions and effects brought by phase and amplitude modulation on quasicrystal arrangement still lack research. Here, we design and fabricate a dielectric quasicrystal metasurface which can simultaneously reconstruct holographic images and exhibit diffraction patterns by assembling the nanostructures in a quasi-periodic array. Most importantly, we combine the global arrangement of metasurfaces with the local responses (phase and amplitude) of meta-atoms for achieving the dual functionality. Furthermore, we also suppress the zero diffraction order in the far-field based on the quasi-momentum matching rule. The proposed method has great mathematical importance and explores new possibilities for multifunctional meta-devices for holographic display, optical switching and anti-counterfeiting.

Keywords Quasicrystal metasurface, Quasi-periodic array, Holography, Diffraction generation, Multifunctional meta-devices

1 Introduction

Metasurfaces, a type of 2D surface composed of artificial subwavelength structures, have shown great potential in manipulating various properties of light (such as amplitude [1, 2], phase [3–5], and polarization [6, 7]) through elaborately engineering meta-atoms. Introducing holographic technology to metasurface promotes the realization of many applications including beam shaping [8–11], optical display [12–16], data storage [12, 17, 18], communication [19–21], cloak [22], and so on. Color hologram [23–26], polarization multiplexing [27–30], and OAM-multiplexing schemes [12, 31–33] are proposed in order to expand the information storage and multifunctional capability of metasurfaces. Traditional metasurfaces are usually arranged in a periodic pattern such as a square or hexagonal lattice, which is one of the forms of a two-dimensional Bravais lattice. In this generalized design strategy, the first step is to calculate the global phase or amplitude profile of metasurface, and in the second step the meta-atoms with suitable local responses are selected [34]. Hence, the current researches on metasurfaces are biased towards the electromagnetic response

*Correspondence:
Lingling Huang
huanglingling@bit.edu.cn
[1] Beijing Engineering Research Center of Mixed Reality and Advanced Display, MIIT Key Laboratory of Photonics Information Technology, School of Optics and Photonics, Beijing Institute of Technology, Beijing 100081, China
[2] Beijing National Laboratory for Condensed Matter Physics, Institute of Physics, Chinese Academy of Sciences, Beijing 100191, China
[3] Laser Micro/Nano-Fabrication Laboratory, School of Mechanical Engineering, Beijing Institute of Technology, Beijing 100081, China

of local nanostructures, and the attentions to the global symmetry of metasurfaces array are insufficient [35]. That is, as one of the essential features of the metasurfaces, the arrangement of meta-atoms has not been exploited in this regard. However, the new approach that combines the global arrangement of metasurfaces with the local responses of meta-atoms may lead to new developments of multifunctional meta-devices.

The periodic latticed crystal exhibits both short-range order and long-range order characteristics. The concept of quasicrystal can be referred to as quasi-periodic and long-range order, which is the logical extension of the notion of a crystal [36]. It was initially identified by the diffraction of metallic solid and the natural quasicrystals were discovered in 2009 [37]. The quasicrystals and their distinctive diffraction patterns have attracted considerable attentions in a variety of domains including chemistry [38], mathematics [39], physics [40], and optics [41]. Numerous unexpected phenomena have been observed by combining quasicrystal structures with other concepts. Unique features such as complete photonic bandgaps [42], localized states [43], and nonlinear effect enhancement [44] have been demonstrated by introducing quasicrystal to photonic crystal. Quasicrystal metasurfaces (QCMs) where meta-atoms are structured in the quasi-periodic lattice have yielded the optical spin-Hall effect [45], broadband polarization conversion [46], and control of nonlinear effects [35] in recent years. Quasicrystal metasurface may develop the new design approach by simultaneously modulate the local phase and amplitude, as well as the arrangement of meta-atoms in different way. Moreover, quasicrystal has a natural advantage in this regard due to its property of long-range order without translational periodicity. However, additional functions and effects brought by local phase and amplitude modulation on quasicrystal arrangement still lack research in previous work.

Here, for the first time, we propose and demonstrate a kind of quasicrystal metasurface that can generate diffraction patterns of quasicrystals and reconstruct holographic images simultaneously. The QCMs are designed by arranging the meta-atoms in the Penrose tiling which can possess the local amplitude and phase response. Due to the quasi-periodic and long-range order of meta-atoms, distinctive diffraction patterns of such QCMs can be observed in the far-field. While the reconstructed image at the predefined distance (either in the Fresnel domain or Fourier domain) is generated based on the phase modulation provided by each meta-atom of QCMs. We fabricate helicity-dependent and birefringent QCM samples according to the geometric phase and propagation phase principle for experimental verifications. Furthermore, a special gradient phase modulation

is also used to suppress the zero diffraction order in one polarization channel of birefringent QCMs, and the holographic images are generated in another channel. Such a concept offers a fresh perspective on quasicrystal metasurface application, as well as provides insightful research of local phase modulation by considering the position arrangement. The demonstrated approach can provide metasurface holographic multiplexing with an additional manipulation dimension including position arrangement and local phase modulation and pave the way for various applications such as holographic display, optical switching, quantum information processing, and anti-counterfeiting.

2 Results

The schematic illustration of the proposed quasicrystal metasurface for simultaneously displaying holographic images and diffraction patterns is shown in Fig. 1. As the fundamental building block of the QCMs, silicon nanofins setting on a quartz substrate are chosen and imprinted in a typical quasi-periodic arrangement of Penrose tiling pattern [47]. The hologram is encoded into the local response of the meta-atoms to compose the phase profile of the QCM, and the holographic image is reconstructed at the predefined distance. Meanwhile, the diffraction pattern which is generated in the far-field is determined by the quasicrystal position arrangement of the QCM. Both the local response of meta-atoms and their arrangement can modulate the transmitted light to achieve such dual functionality. That is, altering the placement of nanostructures while appending additional phase modulation can lead to totally different phenomena compared to traditional diffraction patterns from natural quasicrystal. Hence, distinctive diffraction pattern resulted from the quasicrystal arrangement and preset holographic images can be displayed in the far-field and near-field, respectively. The design details are as follows.

For conventional metasurfaces, the meta-atoms are usually patterned in square or hexagonal periodic lattice, which is particularly convenient for hologram calculation based on 2D Fast Fourier Transform (FFT). In addition, undesired higher diffraction orders are avoided due to the subwavelength pixel size, and the quality of the reconstructed holographic image can be improved. The position of nanoscale optical resonators patterned at the interface, however, has been neglected to a certain extent in metasurface holography. The quasi-periodic lattice lacks short-range order in comparison to the periodic lattice but possesses long-range order. The structure factor obtained by Fourier transform has an unusual n-fold for $n = 5$, 8, 12, and so on, which may reveal rotational symmetry [48]. As a result, the incident light is scattered by
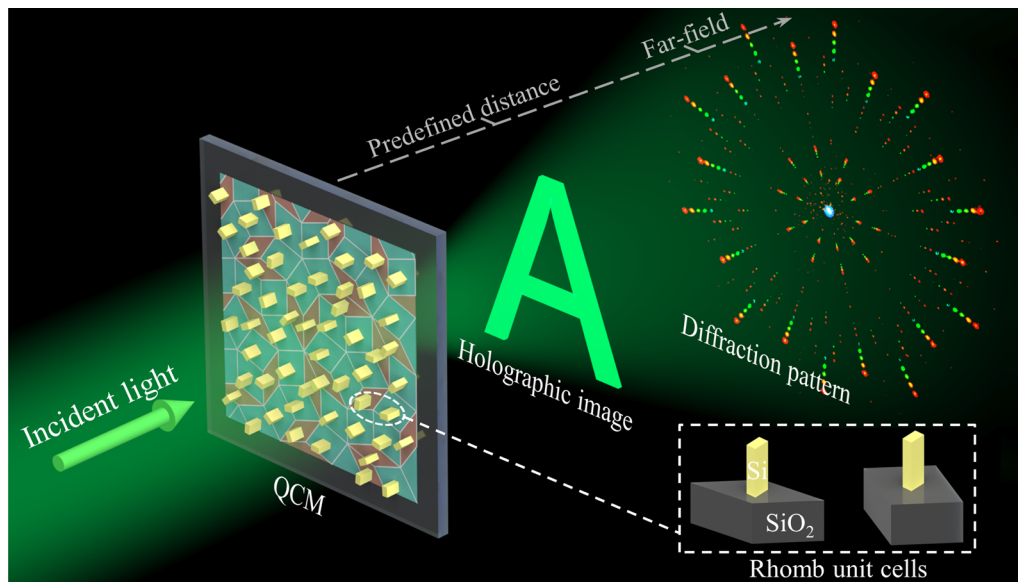
Fig. 1 Schematic illustration of quasicrystal metasurface holography. The demonstrated QCMs can reconstruct holographic images and display diffraction patterns simultaneously. Silicon nanofins are arranged in the Penrose tiling pattern as illustrated by the 2D color image on the surface of the quartz substrate to form the QCM. The letter "A" chosen as a holographic image is reconstructed at the predefined distance by the phase distribution of the QCM. And the far-field diffraction pattern with ten-fold rotation symmetry is generated due to the quasi-periodic array. The unit cells in the bottom right corner indicate the cyan thick rhombus and pink thin rhombus of Penrose tiling

the quasicrystals, creating intricate and stunning diffraction patterns in the far-field. In contrast, periodic arrays in a two-dimensional lattice are limited to a maximum sixfold symmetry due to the crystallographic restriction theorem [49]. For periodic square lattice and hexagonal lattice, only regular and rotationally symmetry limited diffraction patterns can occur.

Here, we design the QCM samples according to the famous Penrose P3 tiling, which is created by using a Robinson triangle decomposition method [50] and based on two types of fundamental building tiles (thick and thin rhombus possess tile side length d with vertex angles of 72° and 36°, respectively). The Penrose tiling is related to the golden ratio $\tau = (1 + \sqrt{5})/2$ according to the Fibonacci sequence. The schematic illustration of the Robinson triangle decomposition method for generating Penrose tiling is shown in Fig. 2a. The thin and thick rhombuses R_A and R_B are the fundamental building tiles of Penrose tiling. Each of the rhombuses is decomposed into two Robinson isosceles triangles (R_A to T_A and $T_{A'}$, R_B to T_B and $T_{B'}$). We set the length of the Penrose rhombus side and the initial Robinson isosceles triangle waist side to d. Then, each Robinson triangle can be substituted by smaller isosceles triangle tiles with a waist side length of d/τ according to its respective decomposition mode. These triangles are reduced by a factor of τ in each decomposition. In this way, unlimited Penrose tiling can be generated and we can make numerous substitutions.

We pattern the silicon nanofins quasi-periodically on the quartz substrate in either vertex sampling or center sampling to form QCMs. In the center sampling case, the meta-atoms are arranged at the center of each rhombus which helps to correlate the position with the rotation angle of the tiling building blocks as shown in Fig. 2b. While, in the vertex sampling case, the nanofins are located at the vertices of each rhombus. The demonstrated quasicrystal metasurfaces based on Penrose tiling have five-fold rotation symmetry which can generate a corresponding ten-fold rotation symmetry diffraction pattern in the far-field.

According to the quasi-momentum conservation rule [48], strong transmission resonances with aperiodic arrangement will be observed for such QCMs. In our demonstrated QCMs, the far-field diffraction occurs under the following conditions:

$$\boldsymbol{k}_{o,\parallel} = \boldsymbol{k}_{i,\parallel} + \boldsymbol{G} \tag{1}$$

where $\boldsymbol{k}_{o,\parallel}$ and $\boldsymbol{k}_{i,\parallel} = 2\pi \sin\theta_i / \lambda$ represent the in-plane wavevector of diffraction beam and incident light, respectively. The angle between the wavevector of incident light and the normal direction of QCMs is θ_i. And λ refers to the wavelength of incident light. It can be obviously seen that $\boldsymbol{k}_{o,\parallel} = \boldsymbol{G}$ for normal incidence. $\boldsymbol{G}$ is the geometrical structure factor of metasurfaces which can be calculated according to any vector in the momentum or reciprocal space by applying Fourier transform to the
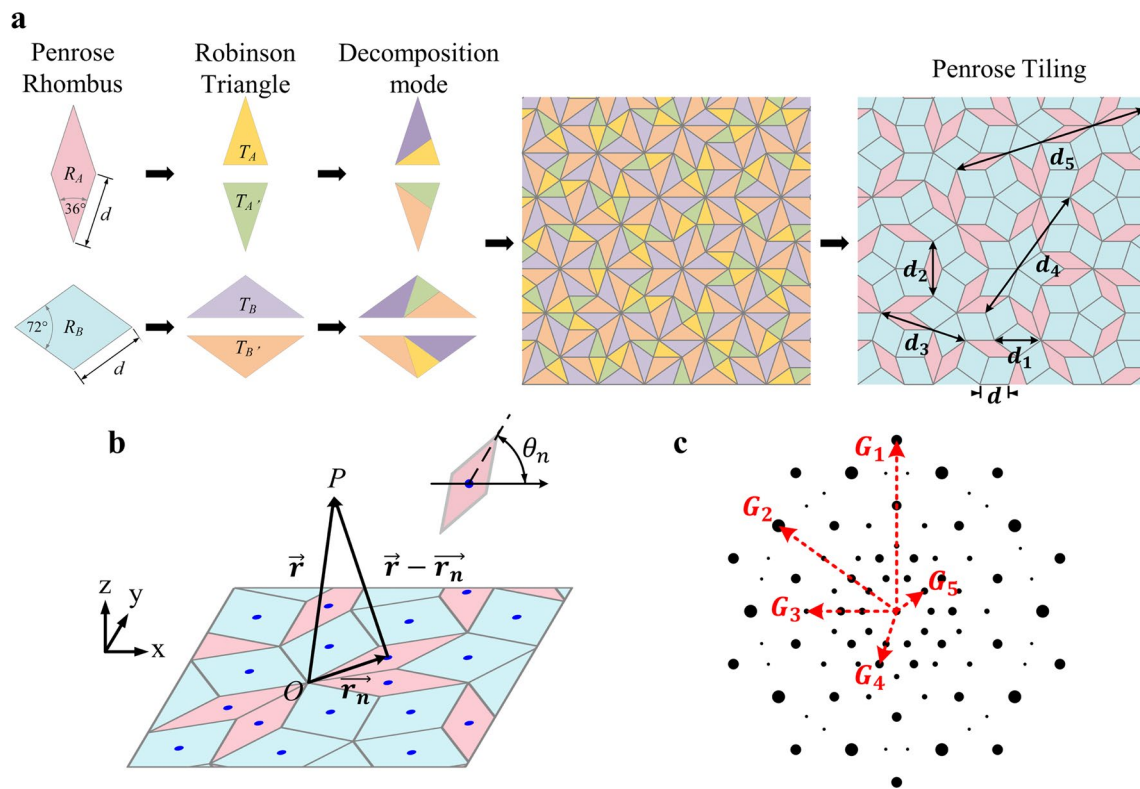
Fig. 2 Schematic illustration of Robinson triangle decomposition method and geometrical structure factor. **a** Robinson triangle decomposition method and characteristic distance of the quasicrystal array. The R_A and R_B are thin and thick Penrose rhombuses with 36° and 72° vertex angles, respectively. And d is the side length of the rhombus. The T_A, $T_{A'}$, T_B, and $T_{B'}$ are Robinson isosceles triangles. **b** Schematic setup of the radiating dipole. r is the vector from the origin O directing to the observation P. θ_n is the rotation angle of the Penrose rhombus. **c** Reciprocal vector of our quasicrystal metasurfaces

positions r_n of meta-atoms in real-space. This is equivalent to the accumulation of radiation from each meta-atom in the far-field. Hence, the diffraction pattern can be obtained as follow [35]:

$$
\begin{aligned}
f(\boldsymbol{k}) &= \mathcal{F}\left[\sum_n \delta(\boldsymbol{r} - \boldsymbol{r}_n)\exp\left(i\varphi_n\right)\right] \\
&= \frac{1}{N}\sum_{n=1}^{N} \exp\left[-i(\boldsymbol{k}\cdot\boldsymbol{r}_n - \varphi_n)\right]
\end{aligned}
\tag{2}
$$

where the meta-atoms are assumed to be dipole emission sources with uniform amplitude. And φ_n is the phase shift which is provided by the meta-atom and $\boldsymbol{k}$ refers the wave vector. The structure factor is also intrinsically connected with the characteristic distance of the quasicrystal array. When φ_n is randomly set, the relation can be expressed as $|\boldsymbol{G}_1| = 4\pi/d_1$, where $d_1 = d\tau$. When the gradient phase is applied, the reciprocal vector of QCMs can be represented as $|\boldsymbol{G}_m| = 4\pi/d_m (m = 1, 2, \ldots, 5)$, where d_1 is the same as before and $d_{2,\ldots,5} = d\{\gamma, \tau^2, \tau^2\gamma, \tau^3\gamma\}$

with $\gamma = \sqrt{\tau + 2}$. The $d_2 \sim d_5$ are new characteristic distance produced by the differences between lattice points [45]. This leads to the emergence of more abundant diffraction levels as shown in Fig. 2c.

On the other hand, the phase distribution of the QCM is obtained from the hologram and is additionally added to each meta-atom that has rarely been applied in traditional quasicrystal. Therefore, the far-field diffraction patterns can be generated by adjusting the positions of meta-atoms while the holographic display can be achieved simultaneously. In this case, the phase modulation of the meta-atoms on the diffraction patterns can be considered random. We can also apply special phase modulation to control the far-field radiation behavior to achieve various functionalities. For example, editing the nanostructures with corresponding gradient phase $\varphi_n = \{0, 2\pi/5, 4\pi/5, 6\pi/5, 8\pi/5\}$ according to the rotation angle of the Penrose rhombus $\theta_n = \{0°, 36°, 72°, 108°, 144°\}$ in center sampling as shown in Fig. 2b. In this way, the zero diffraction order

of the far-field diffraction pattern can be suppressed by a destructive interference caused by combining the global rotation symmetry of metasurface arrangement with the gradient phase modulation.

Based on the above principle, we design a helicity-dependent and a birefringent QCM named Sample 1 and Sample 2, respectively. The flowchart of the modified Gerchberg-Saxton algorithm for generating holograms and designing the quasicrystal metasurface is illustrated in Fig. 3. Unlike the conventional method for generating the hologram with square periodic lattice sampling, the particularity of the Penrose sampling renders it inapplicable for directly employing 2D FFT. Therefore, we improve the GS algorithm to make it suitable for computing holograms of arbitrary arrangements. The Fourier transform used to create an iterative loop between the hologram and image plane to calculate the desired phase profile is

replaced by Kirchoff's diffraction formula. Here, both the hologram and image plane are considered as a collection of distinct point sources. By superimposing all optical wavefronts from the point sources on the image plane, the complex amplitude $A(\xi_l, \zeta_l)$ on the hologram plane can be obtained and vice versa. In this way, the phase-only holograms of arbitrary arrangement can be obtained and encoded into the phase distribution of the QCMs. Moreover, the holographic images can be reconstructed at an arbitrary predefined distance away from the QCMs.

We design two cases for the demonstration of the dual functional quasicrystal metasurface. Sample 1 has only one polarization channel for the reconstruction of holographic images, and the far-field diffraction pattern is generated by the quasi-periodic arrangement. While Sample 2 has two polarization channels for holography display and diffraction pattern generation, respectively.
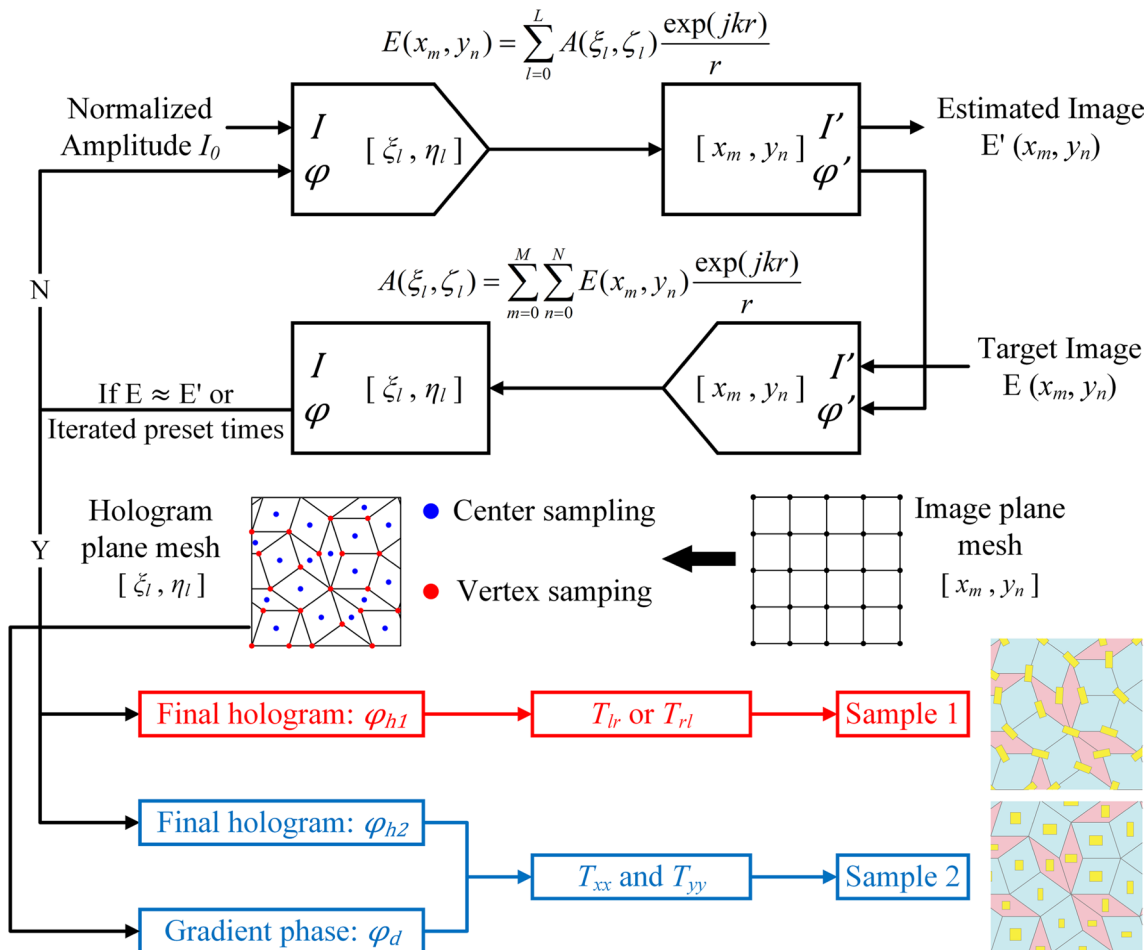
Fig. 3 The flowchart of the modified Gerchberg-Saxton algorithm for generating the holograms and designing the QCMs. The red and blue dots in the hologram plane grid represent the location of the sampling points for vertex sampling and center sampling, respectively. $A(\xi_l, \eta_l)$ and $E(x_m, y_n)$ represent the complex amplitudes of the corresponding positions in the hologram and image planes, respectively. φ_d is the special gradient phase modulation to the far-field diffraction of Simple 2. φ_{h1} and φ_{h2} are the holograms calculated by the modified Gerchberg-Saxton algorithm for Sample 1 and Sample 2, respectively

In contrast to Sample 1, a gradient phase modulation is applied to the extra channel to suppress the zero order of the diffraction pattern. Based on the principle of geometric and propagation phase, the obtained holograms are successfully encoded to Sample 1 and Sample 2, respectively. Meanwhile, vertex sampling and center sampling are adopted for designing Sample 1 and Sample 2. As shown in the illustration of Fig. 3, the QCM Sample 1 consists of rectangular nanofins with the same dimension but different orientation angles which are located at the vertices of the Penrose rhombus. The geometric phase modulation can be expressed as $\varphi = \pm 2\theta$ for different circular polarized incidence, where θ is the rotation angle of the nanofin, and $+$ and $-$ correspond to left-handed and right-handed circular polarization, respectively. Because the geometric phase is wavelength-independent, this QCM may operate across a wide frequency range (see Supplementary Information). For Sample 2, the demonstrated QCM is composed of nanofins with different dimensions but fixed orientation angles which are located at the center of the Penrose rhombuses as shown by the blue points in the hologram plane. By varying the dimensions of the nanofins, the phase shift φ_x and φ_y of two orthogonal linear polarizations can be individually adjusted. In this way, we introduce a special phase modulation to the far-field diffraction of Sample 2 compared to Sample 1. For x-polarized incidence, the phase distribution is selected and the holographic image will be reconstructed at the predefined distance. For y-polarized incidence, the corresponding gradient phase distribution is assigned according to the rotation angle of the rhombuses where the nanofins are located and the quasicrystal diffraction pattern with zero order elimination will be obtained in the far-field.

Then, we fabricated two QCM samples on top of the fused quartz substrate by electron beam lithography for experimental demonstration. The scanning electron microscopy results of the two samples with top view and side view are shown in Fig. 4a–d. The total size of our fabricated QCMs is set at 400×400 μm^2, and the side length of the Penrose rhombus d is set as 1 μm and 0.5 μm for Sample 1 and Sample 2, respectively. Since the lattice period of Sample 1 is longer than the target incident wavelength of 540 nm, more diffraction orders can be observed in the same field of view compared with the target wavelength of 800 nm of Sample 2. We implemented 2D parameter optimization of the rectangular nanofins based on the finite-difference time-domain (FDTD) method to improve the transmission efficiency of Sample 1. Here, we set the length and width of the nanofins to 440 nm and 190 nm, and the height to 1 μm. For the selection of form-birefringent
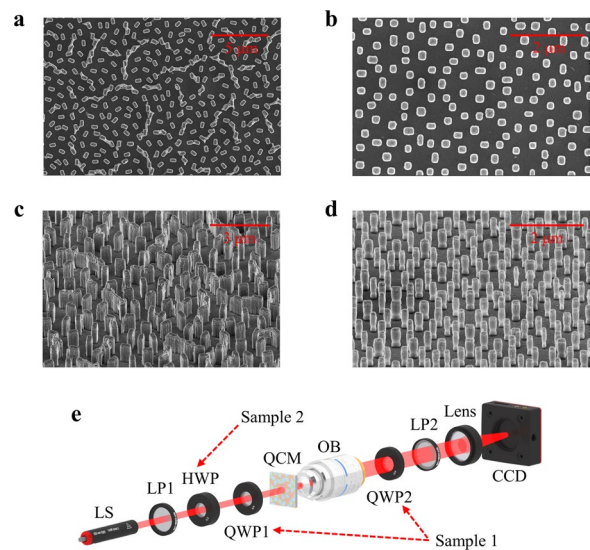
Fig. 4 Scanning electron microscopy images of the fabricated QCM samples and experimental setup. **a**–**d** Scanning electron microscopy images of Sample 1 and Sample 2 are shown with a top and side view. The side length of the Penrose rhombus d is set at 1 μm and 0.5 μm respectively. **e** Experimental setup for observation of the holographic images and diffraction patterns. LS, the laser source; LP1 and LP2, linear polarizers; HWP, half-wave plate; QWP1 and QWP2, quarter-wave plates; QCM, quasicrystal metasurface; OB, objective lens; CCD, charge-coupled device

QCM nanofins of Sample 2, it is required that the phase shift φ_x and φ_y should cover the entire $0 \sim 2\pi$ range and arbitrary phase combinations could be allowed with high transmission. A 2D parameter optimization is carried out by sweeping the length L and width W of the nanofin in the range of $80 \sim 240$ nm with an interval of 10 nm based on a rigorous coupled wave analysis (RCWA) method. While the height of nanofin is set as 600 nm (see Supplementary Information). Furthermore, the deviation between the theoretically calculated phase distribution of hologram and realistic phase response of select nanofins is required to be minimum.

The experimental setup used in the experiment is illustrated in Fig. 4e. The incident light illuminated the sample with desired linear or circular polarization states modulated by polarization optical elements (LP1, HWP, and QWP1). The fabricated QCM samples were placed at the working distance of an objective lens and the transmitted light was finally imaged on a charge-coupled device (CCD) after a lens. Meanwhile, another group of polarization optical elements were used for selecting the polarization states of the hologram and diffraction pattern.
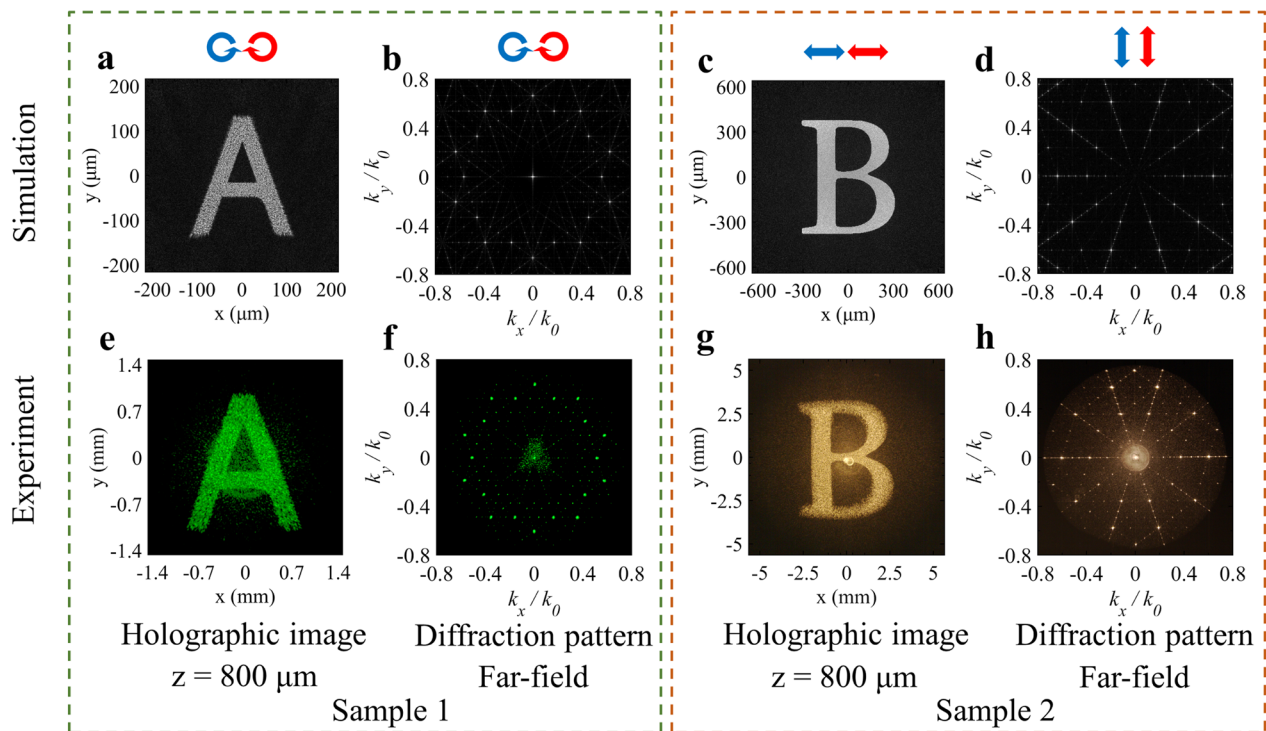
The simulation and experimental results of Sample 1 and Sample 2 are provided in Fig. 5. Note that the simulation results of holographic images are derived from

the scalar diffraction theory. The simulated diffraction patterns are obtained based on Eq. 2. For Sample 1, the polarization state of incident light is left circular polarization (LCP) with a wavelength of 540 nm. And the desired phase modulation is acquired in the cross-polarization channel as depicted in Fig. 5e. The holographic image "A" is successfully reconstructed at a distance of 800 μm away from the QCM. While the quasicrystal diffraction patterns with ten-fold rotation symmetry and unsuppressed zero order can be observed in the far-field. The diffraction pattern of Sample 1 shows more abundant diffraction orders than Sample 2 in the same field-of-view (NA = 0.85) due to the incident wavelength being much less than the quasicrystal lattice period. For Sample 2, the incident and transmitted light have the same linear polarization state (either horizontal or vertical polarization) according to the propagation phase principle (as shown in Fig. 5g, h). In this case, the wavelength of incident light is 800 nm. The holographic image "B" is reconstructed at the same distance of 800 μm in *x*-polarization channel. While in *y*-polarization channel, the gradient phase modulation is imposed and the zero order of the diffraction pattern is well suppressed in the experimental result and fully eliminated in the simulation. The far-field diffraction

of Sample 1 has no such special phase modulation apart from the holographic phase modulation.

In the experiment, the measured transmission efficiency and the polarization conversion efficiency of Sample 1 are 56.12% and 21.77%, respectively. The transmission efficiency and polarization conversion efficiency are defined as the power of all transmitted light and of the holographic image divided by the power of the incident light, respectively. For Sample 2, the measured transmission efficiency of *x*-polarized incidence and *y*-polarized incidence is 70.50% and 46.46%, respectively. The lower efficiency of Sample 1 relative to Sample 2 is mainly caused by the high absorption of silicon material at the working wavelength of Sample 1 and its pitch being larger than the incident wavelength. For Sample 2, the *y*-polarized channel has lower efficiency than the *x*-polarized channel due to the destructive interference. Meanwhile, both Sample 1 and 2 have great broadband properties (see Supplementary Information). The corresponding experimental results and transmission efficiencies are also provided in Supplementary Information.

Furthermore, in order to demonstrate the suppression effect of zero diffraction order in the far-field caused by the introduced phase modulation more clearly,

Fig. 5 Simulated and experimental results for Sample 1 and Sample 2. **a–d** Simulated results of the holographic images and diffraction patterns. **e–h** Experimental results of the holographic images and diffraction patterns. The blue and red arrows represent the polarization state of the incident and transmitted light respectively. Both the holographic images are reconstructed at a distance of 800 μm away from the samples. The diffraction patterns are calculated and captured in the far-field. The wavelengths of incident light for Sample 1 and Sample 2 are 540 nm and 800 nm respectively

helicity-dependent Sample 3 and Sample 4 were fabricated through the center sampling method as a comparison. As shown in Fig. 6a, none of the nanofins of Sample 3 are rotated which indicates that the additional phase modulation was not applied, and only the quasicrystal arrangement contributes to the effect. While the nanofins of Sample 4 are arranged with gradient phase according to the azimuth angle of the rhombus. In this condition, a gradient phase modulation was applied to Sample 4 to eliminate the zero order. As shown in Fig. 6b, e, the zero diffraction orders were clearly observed in the simulated result of Sample 3 and almost completely suppressed in Sample 4. The suppression effect of zero diffraction order makes other diffraction orders exhibit higher energy than Sample 3.

3 Discussion

The quasicrystal metasurface has a wide range of applications, such as holographic anti-counterfeiting. It can meet the full-level requirements of anti-counterfeiting and has strong security and application potential. In fact, the applicability of using the arrangement of meta-atoms as an additional degree of freedom for multiplexing is extremely broad. The introduction of quasi-periodic scheduling into metasurfaces can adapt to almost any function of metasurfaces including holographic displays, metalense, beam generation, and so on. In addition to the practical value of quasicrystal metasurfaces, more importantly, it also gives us inspiration in scientific research. Quasicrystal metasurfaces provide a direct means of combining the global design for meta-atom arrangement surpassing traditional periodic ones, which may trigger the discovery of more novel experimental phenomena and physical properties. Moreover, it may provide a technical means for the detection of substances with special arrangements as well as phases distributions in nature.

In summary, we have proposed a quasicrystal metasurface for dual functionality of holography and generation of distinctive diffraction patterns. By turning the permutation of the meta-atoms into quasi-period, unique quasicrystal diffraction patterns can be observed in the far-field without impeding holographic display. This is because changing the arrangement of meta-atoms only
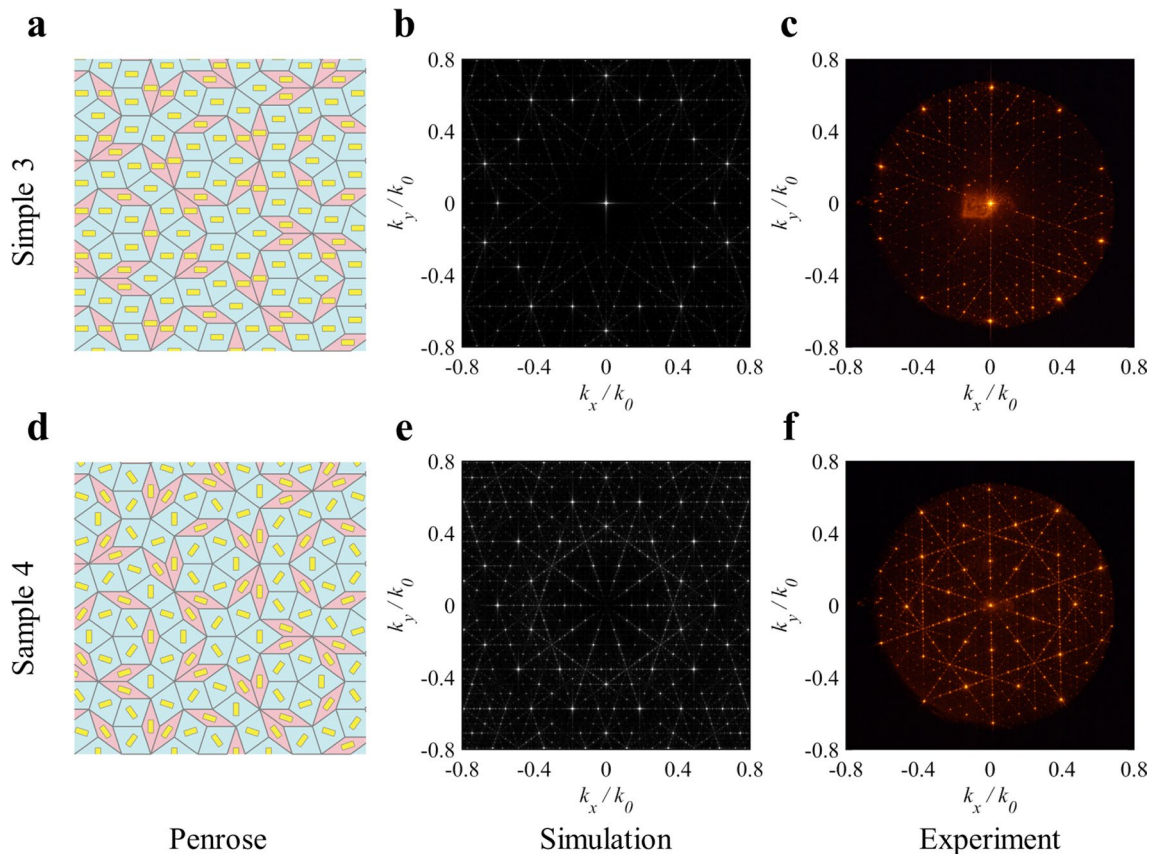
Fig. 6 Simulated and experimental results for Sample 3 and Sample 4. **a** and **d** Schematic diagram of Penrose arrangement quasicrystal metasurfaces. **b** and **c** Simulated and experimental results of diffraction patterns of Sample 3. **e** and **f** Simulated and experimental results of diffraction patterns of Sample 4

affects the reciprocal lattice vector of the metasurfaces, while additional phase modulation is demonstrated for the first time to such quasicrystal metasurfaces for extra functionalities. The demonstrated method has been proved by the theoretical analysis and experimental results in helicity-dependent and birefringent QCMs. Accordingly, a novel holographic algorithm is developed to solve the problem of incompatibility between the special arrangement and traditional hologram calculation method using FFT. Such an algorithm is achieved by interpolating the hologram in quasi-periodic arrangement according to the sampling method. Hence, more functionalities may be opened up by using different quasi-periodic or well-designed arrangements of QCM. Furthermore, applicating additional phase modulation is also one of the ways to control the diffraction patterns. Such work undertakes in-depth research into the important mathematical and physical concept of quasicrystal arrangement with delicately controlled phase distribution, as well as provides a new dimension for metasurface multiplexing technology. The proposed method here may pave the way for optical switching, holographic display, optical encryption, and other light field manipulations.

4 Materials and methods

4.1 Experimental design

We use an experimental setup as shown in Fig. 4e to demonstrate the generation of diffraction patterns and holographic images based on quasicrystal metasurfaces. Supercontinuum laser is applied to provide a different coherent wavelength. A pair of linear polarizers or a combination of linear polarizers and quarter-wave plates are placed in front of and behind the sample to select the desired incident/transmitted linearly/circularly polarized beam. Our quasicrystal metasurface sample is placed at the working distance of the objective lens ($\times 60/$ NA$=0.85$) to guarantee that the Fourier plane is located in the back focal plane. Meanwhile, the magnifying ratio and numerical aperture of the objective lens are carefully chosen to collect all the diffraction light from the sample and reconstruct the holographic images in the predefined plane. Another objective/lens is used for capturing the Fourier plane on a CCD camera. The CCD camera is placed on a moving guide and can be moved around the back focal plane of the imaging lens. The diffraction patterns and the Fourier holographic images are collected at the position of the back focal plane of the imaging lens, and the Fresnel holographic images are captured at a distance in front of the back focal plane.

4.2 Fabrication of the metasurfaces

The fabrication of the quasicrystal dielectric metasurfaces was carried out on a glass substrate, adhering to the steps of deposition, patterning, lift off, and etching. Initially, we used plasma enhanced chemical vapor deposition (PECVD) to deposited the film of amorphous silicon (a-Si) with desired thickness. Subsequently, a poly-methyl-methacrylate (PMMA) resist was applied over the a-Si layer through spin coating, followed by a baking phase at 180 °C for two minutes to expel any solvents. Following this preparation, the target metasurface pattern was created using conventional electron beam lithography, with the pattern then developed in a mixed solution of MIBK and IPA at a 1:3 ratio. After patterning, the specimen was cleansed with IPA and subsequently layered with a 45-nm film of chromium through electron beam evaporation. The subsequent stage entailed a lift-off process, carried out in hot acetone to remove excess material. The process culminated with the employment of inductively coupled plasma reactive ion etching (ICP-RIE), a technique that enabled the transfer of the etched chromium pattern directly onto the silicon layer, creating the final quasicrystal metasurface structure.

Supplementary Information

The online version contains supplementary material available at https://doi.org/10.1186/s43593-024-00065-7.

Supplementary material 1.

Supplementary material 2.

Supplementary material 3.

Supplementary material 4.

Author contributions
L.H. proposed the idea, C.X. and R.Z. conducted pattern designs and numerical simulations, C.X., R.Z. and S.Z. conducted the hologram generation, G.G. J.L. and Xiaowei Li fabricated the samples, C.X., X.Z. and R.Z. performed the measurements, L.H., C.X. and R.Z. prepared the manuscript. L.H., Y.W. and Xin Li supervised the overall project. All of the authors analyzed the data and discussed the results.

Availability of data and materials
The Source data are available from the corresponding author upon request. All data needed to evaluate the conclusion are present in the manuscript and/or the Supplementary Information.

Declarations

Competing interests
The authors declare that they have no competing interests.

References

1. Z. Yue, G. Xue, J. Liu, Y. Wang, M. Gu, Nanometric holograms based on a topological insulator material. Nat. Commun. **8**, 15354 (2017)
2. Q. Fan et al., Independent amplitude control of arbitrary orthogonal states of polarization via dielectric metasurfaces. Phys. Rev. Lett. **125**, 267402 (2020)
3. L. Huang et al., Three-dimensional optical holography using a plasmonic metasurface. Nat. Commun. **4**, 2808 (2013)
4. S. Zhang et al., Nonvolatile reconfigurable terahertz wave modulator. PhotoniX **3**, 7 (2022)
5. G. Zheng et al., Metasurface holograms reaching 80% efficiency. Nat. Nanotechnol. **10**, 308–312 (2015)
6. X. Guo et al., Full-color holographic display and encryption with full-polarization degree of freedom. Adv. Mater. **34**, 2103192 (2022)
7. A.H. Dorrah, N.A. Rubin, A. Zaidi, M. Tamagnone, F. Capasso, Metasurface optics for on-demand polarization transformations along the optical path. Nat. Photonics **15**, 287–296 (2021)
8. J. Yang et al., Generation of the Bessel beam of longitudinally varied polarization with dielectric metasurfaces. Adv. Opt. Mater. **11**, 2202896 (2023)
9. Z. Jin et al., Phyllotaxis-inspired nanosieves with multiplexed orbital angular momentum. eLight **1**, 5 (2021)
10. Y. Hu et al., Dielectric metasurface zone plate for the generation of focusing vortex beams. PhotoniX **2**, 10 (2021)
11. G. Kim et al., Metasurface-driven full-space structured light for three-dimensional imaging. Nat. Commun. **13**, 5920 (2022)
12. H. Ren et al., Complex-amplitude metasurface-based orbital angular momentum holography in momentum space. Nat. Nanotechnol. **15**, 948–955 (2020)
13. R. Zhao, L. Huang, Y. Wang, Recent advances in multi-dimensional metasurfaces holographic technologies. PhotoniX **1**, 20 (2020)
14. Y. Li et al., Ultracompact multifunctional metalens visor for augmented reality displays. PhotoniX **3**, 29 (2022)
15. P. Georgi et al., Optical secret sharing with cascaded metasurface holography. Sci. Adv. **7**, eabf9718 (2021)
16. Y. Yang et al., Integrated metasurfaces for re-envisioning a near-future disruptive optical platform. Light Sci. Appl. **12**, 152 (2023)
17. Y. Chen, X. Yang, J. Gao, 3D Janus plasmonic helical nanoapertures for polarization-encrypted data storage. Light Sci. Appl. **8**, 45 (2019)
18. G.-Y. Lee et al., Complete amplitude and phase control of light using broadband holographic metasurfaces. Nanoscale **10**, 4237–4245 (2018)
19. F. Zhang et al., Holographic communication using programmable coding metasurface. Nanophotonics **13**, 1509–1519 (2024)
20. H.-X. Xu et al., Polarization-insensitive metalens and its applications to reflectarrays with polarization diversity. IEEE Trans. Antennas Propag. **70**, 1895–1905 (2022)
21. H.-X. Xu, Y. Shao, H. Luo, Y. Wang, C. Wang, Janus reflective polarization-division metadevices with versatile functions. IEEE Trans. Microw. Theory Tech. **71**, 3273–3283 (2023)
22. H.-X. Xu et al., Polarization-insensitive 3D conformal-skin metasurface cloak. Light Sci. Appl. **10**, 75 (2021)
23. W. Wan, J. Gao, X. Yang, Full-color plasmonic metasurface holograms. ACS Nano **10**, 10671–10680 (2016)
24. Z. Deng et al., Full-color complex-amplitude vectorial holograms based on multi-freedom metasurfaces. Adv. Funct. Mater. **30**, 1910610 (2020)
25. B. Wang et al., Visible-frequency dielectric metasurfaces for multiwavelength achromatic and highly dispersive holograms. Nano Lett. **16**, 5235–5240 (2016)
26. B. Wang et al., Polarization-controlled color-tunable holograms with dielectric metasurfaces. Optica **4**, 1368 (2017)
27. R. Zhao et al., Multichannel vectorial holographic display and encryption. Light Sci. Appl. **7**, 95 (2018)
28. A. Arbabi, Y. Horie, M. Bagheri, A. Faraon, Dielectric metasurfaces for complete control of phase and polarization with subwavelength spatial resolution and high transmission. Nat. Nanotechnol. **10**, 937–943 (2015)
29. D. Wen et al., Helicity multiplexed broadband metasurface holograms. Nat. Commun. **6**, 8241 (2015)
30. J.P. Balthasar Mueller, N.A. Rubin, R.C. Devlin, B. Groever, F. Capasso, Metasurface polarization optics: independent phase control of arbitrary orthogonal states of polarization. Phys. Rev. Lett. **118**, 113901 (2017)
31. R.C. Devlin, A. Ambrosio, N.A. Rubin, J.P.B. Mueller, F. Capasso, Arbitrary spin-to–orbital angular momentum conversion of light. Science **358**, 896–901 (2017)
32. H. Ren et al., Metasurface orbital angular momentum holography. Nat. Commun. **10**, 2986 (2019)
33. H. Zhou et al., Polarization-encrypted orbital angular momentum multiplexed metasurface holography. ACS Nano **14**, 5553–5559 (2020)
34. S. So, J. Mun, J. Park, J. Rho, Revisiting the design strategies for metasurfaces: fundamental physics, optimization, and beyond. Adv. Mater. **35**, 2206399 (2023)
35. Y. Tang et al., Quasicrystal photonic metasurfaces for radiation controlling of second harmonic generation. Adv. Mater. **31**, 1901188 (2019)
36. D. Levine, P.J. Steinhardt, Quasicrystals: a new class of ordered structures. Phys. Rev. Lett. **53**, 2477–2480 (1984)
37. L. Bindi, P.J. Steinhardt, N. Yao, P.J. Lu, Natural quasicrystals. Science **324**, 1306–1309 (2009)
38. M. Yoshimura, A.P. Tsai, Quasicrystal application on catalyst. J. Alloy. Compd. **342**, 451–454 (2002)
39. N.G. De Bruijn, Algebraic theory of Penrose's non-periodic tilings of the plane. I. Indagationes Math. (Proc.) **84**, 39–52 (1981)
40. S. Longhi, Topological phase transition in non-hermitian quasicrystals. Phys. Rev. Lett. **122**, 237601 (2019)
41. Z.V. Vardeny, A. Nahata, A. Agrawal, Optics of photonic quasicrystals. Nat. Photon **7**, 177–187 (2013)
42. M.E. Zoorob, M.D.B. Charlton, G.J. Parker, J.J. Baumberg, M.C. Netti, Complete photonic bandgaps in 12-fold symmetric quasicrystals. Nature **404**, 740–743 (2000)
43. C. Lin, P.J. Steinhardt, S. Torquato, Light localization in local isomorphism classes of quasicrystals. Phys. Rev. Lett. **120**, 247401 (2018)
44. R. Lifshitz, A. Arie, A. Bahabad, Photonic quasicrystals for nonlinear optical frequency conversion. Phys. Rev. Lett. **95**, 133901 (2005)
45. I. Yulevich et al., Optical mode control by geometric phase in quasicrystal metasurface. Phys. Rev. Lett. **115**, 205501 (2015)
46. M.-E. Mustafa, M. Amin, O. Siddiqui, F.A. Tahir, Quasi-crystal metasurface for simultaneous half- and quarter-wave plate operation. Sci. Rep. **8**, 15743 (2018)
47. R. Penrose, Pentaplexity a class of non-periodic tilings of the plane. Math. Intell. **2**, 32–37 (1979)
48. T. Matsui, A. Agrawal, A. Nahata, Z.V. Vardeny, Transmission resonances through aperiodic arrays of subwavelength apertures. Nature **446**, 517–521 (2007)
49. H. Hiller, The crystallographic restriction in higher dimensions. Acta Crystallogr. A Found. Crystallogr. **41**, 541–544 (1985)
50. W. Steurer, S. Arlitt, Kurt Bruckner's view on the Penrose tiling. Struct. Chem. **28**, 51–56 (2017)